LAMINAR-TO-TURBULENT TRANSITION OF $M = 0.8$ BOUNDARY LAYER OVER A HEATED/COOLED FLAT PLATE

Yuta Iwatani
Department of Aerospace Engineering
Tohoku University
Sendai, Miyagi, 980-8579, Japan
yuta.iwatani@dc.tohoku.ac.jp

Hiroyuki Asada
Department of Aerospace Engineering
Tohoku University
Sendai, Miyagi, 980-8579, Japan
h.asada@tohoku.ac.jp

Soshi Kawai
Department of Aerospace Engineering
Tohoku University
Sendai, Miyagi, 980-8579, Japan
kawai@tohoku.ac.jp

ABSTRACT

The impacts of wall temperature on the laminar-turbulent transition of Mach number $M = 0.8$ boundary layer over a flat plate are numerically investigated using direct numerical simulations. Three different isothermal conditions, pseudo-adiabatic and 10% cooled and heated walls, are considered. We introduce tiny disturbances at the specified frequencies aiming to induce the H-type transition. The wall temperature is found to affect the modal growth of the velocity disturbances, thereby influencing the flow structures that appear in the transitional regime and the meanflow characteristics. Wall cooling impedes the growths of the Tollmien–Schlichting (TS) wave, the subharmonic three-dimensional oblique wave, and the steady streaks. In particular, as the TS wave is suppressed well with wall cooling, the streak mode instead becomes dominant like the oblique transition. The three-dimensional flow structures become elongated in the streamwise direction, narrower in the spanwise direction, and flattened in the wall-normal direction with wall cooling. Conversely, wall heating promotes the modal growth of the disturbances and also causes the three-dimensional flow structures to shrink in the streamwise direction and to stretch in the spanwise and wall-normal directions. These three-dimensional structures deviate the skin friction profiles and shape factor from their laminar values. Moreover, it is observed that wall cooling leads to a two-stage evolution of skin friction and shape factor profiles, correlating with the lag in the onset of inflection points near displacement thickness and the boundary between the free stream flow and the viscosity affecting flow.

INTRODUCTION

This study is firstly motivated by the study of Reshotko (1979) who proposed the Hydrogen-Fueled Aircraft equipped with the drag reduction function achieved by cooling the surface with fuel to suppress boundary layer transition. Based on some linear stability analyses, Reshotko estimated that 20% drag reduction would be possible in a cruise condition at Mach number 0.85. This estimation is attractive for the industrial application, however, the wall temperature effects on the late stage of the transition where the disturbances grow enough to interact with each other nonlinearly were not considered.

According to Morkovin (1969), the routes to turbulence bifurcates depending on the initial disturbance level. In a low-level disturbance such as a flight condition, the transition type can be classified into either K-type (Klebanoff *et al.*, 1962; Rist & Fasel, 1995), H-type (e.g. Kachanov & Levchenko, 1984; Fasel *et al.*, 1990), O-type (Schmid & Henningson, 1992; Berlin *et al.*, 1994), or their mixed type. Both the K-type and H-type transitions originate from the planer Tollmien-Schlichting (TS) wave and the three-dimensional oblique waves with a single frequency and wavenumber, but the frequency of the oblique wave differs; the frequency of the oblique wave is the same as the TS wave in the K-type whereas it is half in the H-type. On the other hand, the O-type transition, also referred to as oblique transition, does not need the TS wave but only the oblique wave to occur. The nonlinear triad interaction of a pair of oblique waves with the opposite sign of spanwise wavenumber yields a streamwise vortex. The streamwise vortex yields the streaks via the lift-up effect, which grow downstream rapidly in a manner of a non-modal growth due to the non-normality of the shear flow (Trefethen *et al.*, 1993; Hanifi *et al.*, 1996) to trigger the breakdown to turbulence. In particular, for compressible flows, since the most unstable wave is inclined to the flow direction (Mack, 1984) unlike incompressible flows, this three-dimensional unstable wave has the potential to cause a dominant streak structure and result in the O-type transition. Moreover, owing to a large amplification mechanism of non-modal growth of the streak, the amplitude of the initial oblique wave can be much smaller than in other scenarios for the eventual breakdown to occur (Chang & Malik, 1994). Therefore, it is crucial to take account into the O-type mechanism when considering a compressible boundary transition. Though as such the transition scenario has a variety, Berlin *et al.* (1999) discussed that the amplification mechanism in the late stage of the transition is similar regardless of the scenario; the Λ-shaped vortices and streaks grow through the lift-up effect. The differences come from the energy balance contained in the TS wave, the oblique wave, and the steady streak. In the present study, we choose to compute the H-type transition as it is more likely to occur than the K-type due to the higher growth rate (Herbert, 1988) and the H-type transition includes the lift-up mechanism crucial in the O-type transition as well.

Here, we briefly review the wall temperature effects on the stability of a transonic boundary layer. One of the earliest works concerning the wall temperature effects on the stability of the compressible boundary layer was made by Lees & Lin (1946). They found that the generalized inflection point corresponds to the inflection point in incompressible flows, and theoretically showed that wall cooling stabilizes the boundary layer to the inviscid disturbances. Concerning the viscous instability, Mack (1984) performed the linear stability analyses and revealed that the low-frequency first mode, the counterpart of the TS wave in incompressible flows, is stabilized with wall cooling in the compressible flows. In the H-type transition, the secondary instability of the subharmonic oblique wave on the TS wave plays an important role (Herbert, 1988). Masad *et al.* (1992) performed the Floquet analyses and showed that the secondary unstable subharmonic oblique wave at a low spanwise wave number is stabilized with wall cooling, but the subharmonic wave at a high spanwise wave number is destabilized. The effect of wall temperature on oblique transitions has not been mentioned much and has not been fully elucidated, so there is still room for further clarification. Recently, improvements in computer performance have made it possible to perform direct numerical simulations (DNS) to study the effects of wall temperature on boundary layer transitions in more detail. However, the majority of research efforts regarding the effects of wall temperature on compressible boundary layer transition have been focused on hypersonic boundary layers, aimed at understanding the wall temperature impacts on Mack's second mode (e.g. Unnikrishnan & Gaitonde, 2021). For a supersonic flow, Shadloo & Hadjadj (2017) conducted the DNSs of the transition over a strongly heated-/cooled wall and showed that wall heating stabilizes the flow contradicting the prior studies. Interestingly, the following research by Sharma *et al.* (2018) has concluded that the wall temperature effect switches depending on the amplitudes of initial disturbances; the wall heating stabilizes the disturbances with amplitudes above 1%, but the detailed mechanism remains unclear. Moreover, Masad *et al.* (1992) reported that wall heating/cooling is more effective in destabilizing/stabilizing the flow at the transonic Mach number, the subject of this study, than the high Mach number, therefore it is worth investigating the wall temperature effects on the transonic boundary layer using DNS.

In this study, we conduct the DNS study of the boundary layer transition of transonic over a heated/cooled flat plate to elucidate the wall temperature effects and the mechanism relevant to the promotion or delay of turbulence onset. In the subsequent sections, after describing the numerical methodology and case setup, we visualize and mention the differences in the streamwise development of flow structure and mean flow resulting from wall heating/cooling. The causes of observed differences are explained by correlating to those of the modal growth of velocity disturbances and thereby emerging inflectional instability, triggered by the wall heating/cooling.

METHODOLOGY AND FLOW PARAMETERS

This study directly solves the three-dimensional compressible Navier–Stokes equations:

$$\frac{\partial \rho}{\partial t} + \frac{\partial (\rho u_j)}{\partial x_j} = \sigma_\rho, \tag{1}$$

$$\frac{\partial \rho u_i}{\partial t} + \frac{\partial (\rho u_i u_j)}{\partial x_j} + \frac{\partial P}{\partial x_i} + \frac{\partial \tau_{ij}}{\partial x_j} = \sigma_{\rho u_i}, \tag{2}$$

$$\frac{\partial E}{\partial t} + \frac{\partial ((E+P)u_j)}{\partial x_j} + \frac{\partial u_i \tau_{ij}}{\partial x_j} + \frac{\partial q_j}{\partial x_j} = \sigma_E, \tag{3}$$

where $(x_1, x_2, x_3) = (x, y, z)$ are the streamwise, wall-normal, and spanwise directions, and (ρ, u_i, P) are the density, velocity, and pressure. $E = P/(\gamma-1) + \rho u_i u_i/2$ is the total energy where γ $(= 1.4)$ is the specific heat ratio of the air. σ are the external forcings for the numerical sponge (Mani, 2012). The details of the sponge are provided later. The equations are made non-dimensional by the distance from the leading edge of the flat plate $L = 10^5$, the free density ρ_∞, the speed of sound a_∞, and the viscosity $\mu_\infty = 8 \times 10^{-6}$ where subscript ∞ denotes the free stream value. To close the equations, the ideal gas law $P = \rho R T$, where R is gas constant, and Sutherland law $\mu = (T/T_\infty)^{3/2}(T_\infty + T_1)/(T + T_1)$ where $T_\infty = 255K, T_1 = 110.4K$, are considered. τ_{ij} and q_j are the viscous stress tensor and heat flux vector, respectively, evaluated as

$$\tau_{ij} = \mu \left(\frac{\partial u_i}{\partial x_j} + \frac{\partial u_j}{\partial x_i} - \frac{2}{3}\frac{\partial u_k}{\partial x_k}\delta_{ij} \right), \tag{4}$$

$$q_j = -\frac{\mu}{Pr(\gamma-1)}\frac{\partial a^2}{\partial x_j}, \tag{5}$$

where $Pr(= 0.72)$ is the Prandtl number, a is the speed of sound, and δ_{ij} is the Kronecker delta.

The sixth-order compact scheme is used for spatial discretization with the eighth-order compact low-pass filter (Lele, 1992; Gaitonde & Visbal, 1999). The four-stage fourth-order Runge–Kutta method is adopted for the time integration with the nondimensional time step $\Delta t u_\infty / L = 4.5 \times 10^{-5}$.

Figure 1 shows the schematic of the computational domain. The boundary layer develops spatially over a nominally zero-pressure-gradient flat plate. The free stream Mach number M_∞ is 0.8. We concern the three distinct wall temperature conditions: pseudo-adiabatic (AD) ($T_{\mathrm{wall}} = T_r$), 10%-heated (HE) ($T_{\mathrm{wall}} = 1.1T_r$), and 10%-cooled (CO) ($T_{\mathrm{wall}} = 0.9T_r$) where T_r is the recovery temperature of laminar boundary layer:

$$T_r = 1 + \sqrt{Pr}\frac{\gamma-1}{2}(M_\infty^2 - 1). \tag{6}$$

As the inflow boundary condition, the isothermal wall compressible Blasius solution corresponding to each wall temperature condition is used. To induce the H-type transition,

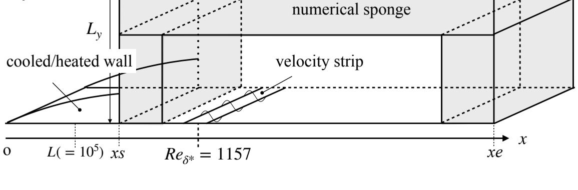

Figure 1. Schematic of computational domain.

we provide tiny wall-normal velocity disturbances v at the wall. The provided disturbance consists of a planer Tollmien–Schlichting (TS) wave and a sub-harmonic three-dimensional oblique wave, written in blowing and suction form as

$$v(x,z) = A_1 f(x)\sin(\omega_1 t) + A_2 f(x) g(z)\sin(0.5\omega_1 t), \quad (7)$$

where $f(x) = 15.1875\xi^5 - 35.437\xi^4 + 20.25\xi^3$, and $g(z) = \cos(2\pi z/\lambda_z)$ (Huai et al., 1997). ξ is the local coordinate in the streamwise direction within the disturbance strip where $x_1 \leq x \leq x_2$, ranging from 0 to 1. The amplitudes of the fundamental TS wave A_1 and the subharmonic oblique wave A_2 are set as $0.0015U_\infty$ and the half of A_1, respectively. These values are consistent with the previous DNS of the H-type transition by Sayadi *et al.*, (2013). The frequency ω_1, the strip width x_1, x_2, the strip station $x_{\text{dist}} := 0.5(x_1 + x_2)$ and the spanwise wavelength λ_z are designed based on the neutral curves as in White & Majdalani (2006). The strip location x_{dist} is determined such that x_{dist} is fixed at $Re_{\delta^*} = 1157$ for all the case where δ^* is the displacement thickness, being computed as

$$\delta^* = \int_0^\infty \left(1 - \frac{\rho(y)}{\rho_\infty}\frac{u(y)}{u_\infty}\right) dy, \quad (8)$$

using the isothermal Blasius solution. The angular frequency $\omega/(u_\infty/L)$ is 4.96 and the spanwise wavelength of the subharmonic wave λ_z/L is 0.33. The width of the strip of the streamwise direction is determined to keep $2\pi\delta^*_{x\text{dist}}/(x_2 - x_1) = 0.18$ for all the cases where $\delta^*_{x\text{dist}}$ is the displacement thickness at the strip station, which results in the different widths in terms of x depending on the wall temperature (see Table 1). The computational domain ranges $0 \leq y \leq 2.0L$ for the wall-normal and $0 \leq z \leq 0.99L$ for the spanwise directions, which contains three subharmonic waves. The inlet and outlet boundaries (xs, xe) are $(1.42L, 20L)$ (He), $(2.0L, 20L)$ (AD), and $(2.79L, 23L)$ (CO). The domain sizes for the streamwise direction are large enough for the boundary layer to fully develop into the turbulent flow. The grid spacings in viscous units are $\Delta x^+ \lesssim 5.2,\ 6.9,\ 5.0$, $\Delta y_w^+ \lesssim 0.3, 0.35, 0.3$, and $\Delta z^+ \lesssim 4.8, 4.8, 5.3$, for the heated, adiabatic, and cooled cases, respectively (see Table 1).

As shown in Figure 2, the numerical sponge is imposed for the inlet, outlet, and top free-stream boundaries by adding the source terms to the governing equations in Equations (1)-(3) to prevent the unphysical pressure wave's reflection at the computational boundaries. Based on the criteria proposed by Mani (2012), the lengths of the sponge are determined as $0.8L$ for the inlet boundary, $1.3L$ for the outlet boundary, and $1.0L$ for the free stream boundary with the source terms σ that can achieve 50dB damping of the acoustic waves for each direction.

Table 1. Parameters depending on the wall temperature.

Case	Tw/Tr	x_{dist}	$(xs,\ xe)$	$\Delta x^+_{\max}$	$\Delta y^+_{w,\max}$	$\Delta z^+_{\max}$
HE	1.1	2.82	$(1.42, 20)$	5.2	0.30	4.8
AD	1.0	3.40	$(2.0, 20)$	6.9	0.35	4.8
CO	0.9	4.19	$(2.79, 23)$	5.0	0.30	5.3

RESULTS OF DNS AND DISCUSSION
Streamwise Evolution of Flow Structure and Meanflow

Figure 2 visualizes the isosurfaces of the second invariants of the velocity gradient tensor obtained in the present DNSs. For all the cases, the staggered Λ-shaped vortices typical in the H-type transition are observed. As growing downstream, they form the hairpin packets and break down to the turbulence. It is observed that these flow structures are affected by the wall temperature. The wall heating stretches the vortices in the wall-normal and the spanwise direction; the legs of the Λ-shaped and hairpin vortices are widely spread and lifted, compared to the other cases. In contrast, the wall-cooling elongates, flattens, and shrinks the vortex structures in streamwise, wall-normal, and spanwise directions.

Figure 3 shows the skin friction coefficient C_f as a function of the streamwise location x. The obtained C_f profiles first follow that of the Blasius solutions and then begin to depart from them around $x/L \approx 5.8, 6.6$, and 8.4 for the heated, adiabatic, and cooled cases, respectively. These locations coincide with the appearance of three-dimensional structures (see also Figure 2). Once the C_f profiles depart from their laminar values, they increase rapidly and show striking overshoots. They reach their peak values at $x/L \approx 8.0$ (HE), 8.9 (AD), and 11.5 (CO). This overshoot of the skin friction profiles has been observed in the prior study of the controlled transition (Sayadi et al., 2013). In particular, Sayadi et al. (2013) discussed that the C_f profile is a good indicator to classify the transition stage into laminar, transitional, and turbulent regimes, which are divided by the start and end location of the increase in skin friction. In Figure 4, we also take a look at the shape factor H (the ratio of the displacement thickness to the momentum thickness), which is also often used to detect the change of boundary layer state because of the transition or the separation. This study computes the shape factor by the method of (Spalart & Watmuff, 1993; Coleman *et al.*, 2018) that evaluates $H = \delta^*_{inc}/\theta_{inc}$ where

$$\delta^*_{inc}(x) = \frac{-1}{\tilde{U}_e(x)}\int_0^\infty y\omega_z(x,y)dy, \quad (9)$$

$$\theta^*_{inc}(x) = \frac{2}{[\tilde{U}_e(x)]^2}\int_0^\infty y\tilde{U}(x,y)\omega_z(x,y)dy - \delta^*_{inc}(x), \quad (10)$$

with the generalized streamwise velocity (Lighthill, 1963)

$$\tilde{U}(x,y) = -\int_0^y \omega_z(x,y')dy',\ \omega_z = \frac{\partial v}{\partial x} - \frac{\partial u}{\partial y}, \quad (11)$$

which can incorporate the effect of pressure gradient. Though this study considers the nominally zero-pressure-gradient flat plate, the pressure gradient is induced by the occurrence of Λ-shaped and hairpin structures in the transition regime. Note that this formulation assumes the incompressible boundary layer and therefore the effect of the density variation is not considered. The dependence of viscosity on the temperature is not considered either, although these thermodynamic property variations are not significant for the cases investigated in this study. Nevertheless, the shape factor of each case is kept constant at about the theoretical value 2.59 (derived from incompressible Blasius solution) in the laminar regime, then begins to decrease in the transitional region, and finally shows an asymptotic approach to the theoretical value of the incompressible turbulent boundary layer near the laminar-turbulent

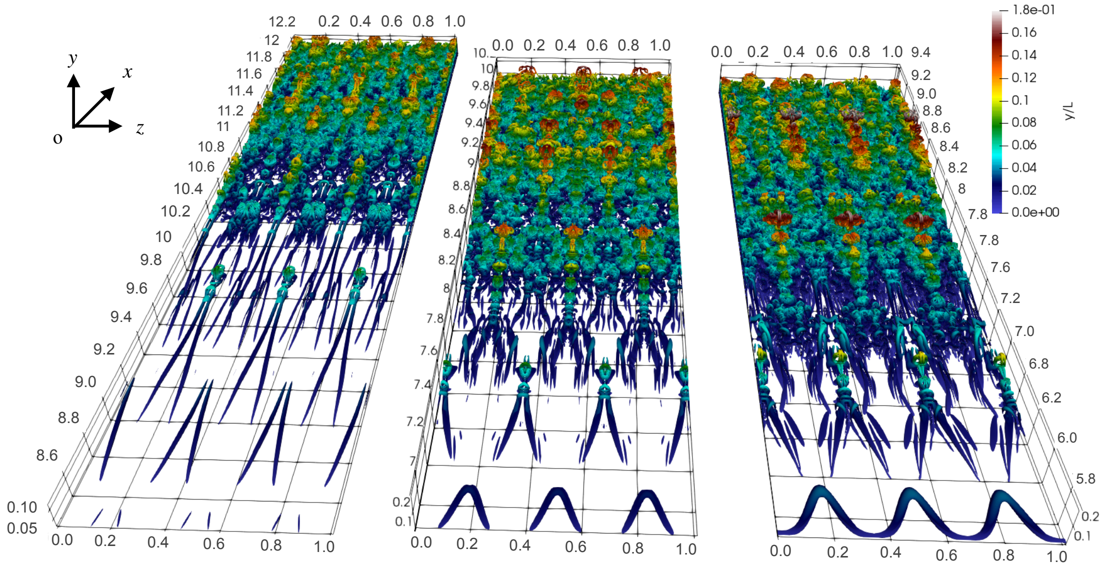

Figure 2. Instantaneous isosurfaces of the second invariant of the velocity gradient tensor near peak location of the skin friction coefficient, colored by the height from the wall. Cooled, adiabatic, and heated cases are shown from left to right.

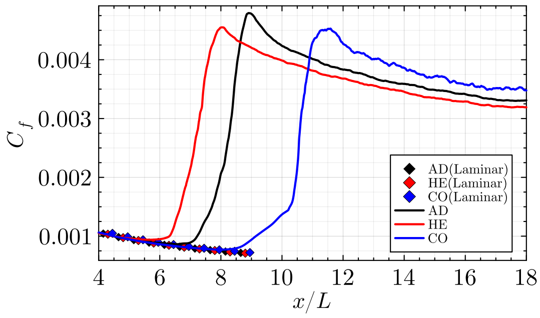

Figure 3. Streamwise distributions of skin friction coefficient as a function of x. The flat plate formula $C_{f,lam} \approx 0.664\sqrt{C^*}/\sqrt{Re_x}$ where $C^* = (0.5 + 0.039M_\infty^2 + 0.5T_{wall}/T_\infty)$ (White, 2006; Eckert, 1955) for each temperature condition is also plotted by the filled diamond.

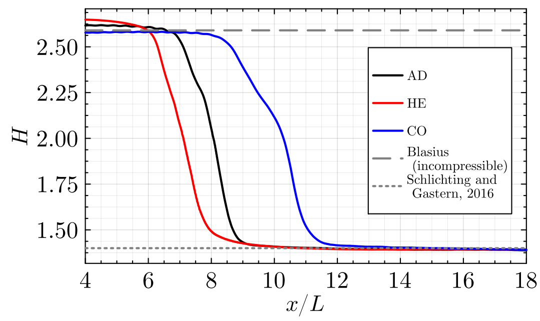

Figure 4. Shape factor as a function of x. The upper dashed line is the theoretical value of the Blasius solution, 2.59, while the lower one is for the turbulent boundary layer 1.4 (Schlichting & Gersten, 2016).

transition 1.4 (Schlichting & Gersten, 2016). This suggests that the shape factor is also a good indicator to classify the boundary layer state.

The effect of the wall heating/cooling on these streamwise distributions of the skin friction coefficient and the shape

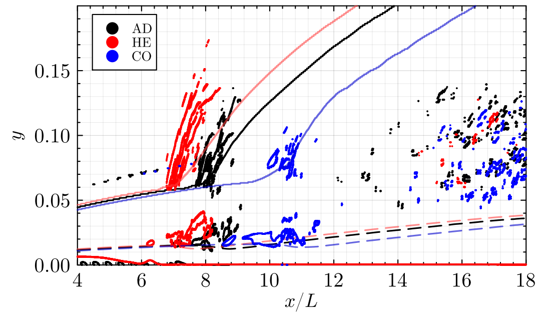

Figure 5. Scatter plots of generalized inflection point. The solid and dash lines indicate the boundary at the freestream $\delta_{inc} + \delta^*_{inc}$ and displacement thickness δ^*_{inc}, respectively.

factor is distinct, especially for the wall-cooling case. Interestingly, the skin friction coefficient and the shape factor seem to change in two stages. As for the skin friction coefficient, the slope of the increase is moderate at first compared to the heated and adiabatic cases, then the slope becomes steep near $x/L \approx 10.5$. We find that such a two-stage variation of the skin friction profile (and shape factor) is related to the presence of the generalized inflection point (GIP). We search for the GIP in a way that the wall-normal height y_{GIP} satisfies

$$\frac{d}{dy}\left(\rho \frac{\partial \bar{u}}{\partial y}\right)\bigg|_{y_{GIP}} = 0. \tag{12}$$

The obtained GIPs are plotted in Figure 5 with the streamwise evolution of the displacement thickness and the sum of displacement thickness and boundary layer height. As shown in Figure 5, almost all the GIPs are found in a transitional region. In addition, the GIPs are concentrated near the line of displacement thickness δ^* or the line of $\delta + \delta^*$ (the boundary between the freestream flow and the viscosity affecting flow). For the heated and adiabatic cases, the GIPs around δ^* and those around $\delta + \delta^*$ appear almost simultaneously $x \approx 6.8, 7.5$, respectively. On the other hand, for the cooled case, there are some lags from the appearance of the GIPs around δ^*

($x/L \approx 8.5$) to that around $\delta + \delta^*$-scale ($x/L \approx 10.0$). This lag of the emergence of the two different height scale GIPs, or the lag of the onset of the inflectional instability, causes the two-stage variation of the skin friction profile. Indeed, the emergence of the GIPs around δ^* almost coincides with the start location of the rise in skin friction ($x/L \approx 8.5$), and that around $\delta + \delta^*$ does with where the slope becomes steeper ($x/L \approx 10.5$, immediately downstream of the presence of the GIPs around $\delta + \delta^*$). Based on the observations of the flow structures shown in Figure 2, the GIPs around $\delta + \delta^*$ are related to the hairpin structures. The relation between GIPs near δ^* and the flow structure is discussed in the next section. Note that there are always GIPs very near the wall for the heated case, while most of them are canceled by wall cooling.

Modal Growth and Relations to Flow Structure and Mean Flow

We conduct the Fourier analyses to understand how the provided disturbances grow in the boundary layer. The streamwise velocity component is Fourier transformed as

$$u'(x,y,z,t) = \sum_{k=-K}^{K} \sum_{h=0}^{H} \hat{u}_{h,k_z}(x,y) e^{i(\omega_1 ht + \beta kz)}, \qquad (13)$$

where (h,k) are the harmonics wavenumbers of the fundamental frequency ω_1 and spanwise wavenumber $\beta = 2\pi/\lambda_z$. For instance, the provided TS component corresponds to $(h,k) = (1,0)$ mode and the subharmonic oblique wave corresponds to $(1/2,1)$ mode. Figure 6 compares the $y-$maxima of the Fourier amplitudes of $(1,0),(1/2,1)$ and $(0,2)$ modes in laminar and transitional regimes of each wall temperature conditions. Here, mode $(0,2)$ is known as the vortex-streak mode, which is generated by a triadic interaction of the subharmonic oblique mode, i.e., $(1/2,1)-(1/2,-1)=(0,2)$. Physically, the vortex-streak mode $(0,2)$ corresponds to the pair of the counter-rotating streamwise vortices, which yields the streak (Berlin *et al.*, 1999).

First, as shown in Figure 6 (a,b), the TS mode $(1,0)$ shows the monotonically exponential growth in the laminar region and then it saturates at $4-10\%$, for the adiabatic and heated cases. For the cooled case in Figure 6 (c), on the other hand, although the TS mode grows exponentially (but slightly) at first, it finally begins to decay from $x/L \approx 7.5$. The amplification ratio of the TS wave $\alpha_{1,0}$ is approximated as $0.18, 0.20$, and 0.03 for the adiabatic, heated, and cooled cases (see Figure 6); the TS wave is suppressed with wall cooling in this study. This result is qualitatively consistent with the neutral curve used to design the disturbance wavelength.

Next, the subharmonic oblique mode $(1/2,1)$ decays initially, but turns to grow as the TS mode grows. That is, the subharmonic secondary instability occurs. For all the cases, the secondary instability occurs where the TS mode's amplitudes reach about $1.0-1.1\%$. This is slightly higher than the threshold amplitude of the TS wave 0.5% for the onset of the subharmonic secondary instability in a (relatively low Mach number) supersonic boundary layer (Chang and Malik, 1993). The growth rates of subharmonic oblique mode $\alpha_{1/2,1}$ are about $1.0, 1.4$, and 0.7 for the adiabatic, heated, and cooled cases, respectively. Thus the subharmonic oblique mode $(1/2,1)$, with the low spanwise wavenumber, is confirmed to be increased/decreased with wall heating/cooling consistently with Masad and Nayfeh (1991).

Finally, the amplitude of the vortex-streak mode $(0,2)$ generated by the oblique wave mode is on order 10^{-3} initially, and then it rapidly grows at a constantly steep slope in all the cases. The computed growth ratios $\alpha_{0,2}$ are 2.0, 2.4, and 1.3 for the adiabatic, heated, and cooled cases, respectively. In other words, wall heating promotes the growth of vortex-streak mode while wall cooling impedes it. Interestingly, however, this vortex-streak mode $(0,2)$ finally exceeds the other modes only when the wall is cooled despite the low growth rate. This infers that the growth mechanism of disturbances for O-type transition becomes comparable to or dominates that of the H-type transition mechanisms as a consequence of the well-suppressed TS $(1,0)$ and the subharmonic oblique $(1/2,1)$ modes by cooling the wall.

In summary, let us revisit the wall temperature impacts on the vortex structure shown in Figure 2. The reason why wall cooling flattens the Λ-shaped and hairpin vortices compared to other wall temperature cases is that it weakens the growth of the vortex streak mode $(0,2)$ responsible for the lift-up mechanism. Conversely, wall heating promotes the growth of $(0,2)$ mode, lifting the structures. In this perspective, a pertinent question arises: Can the deformed three-dimensional struc-

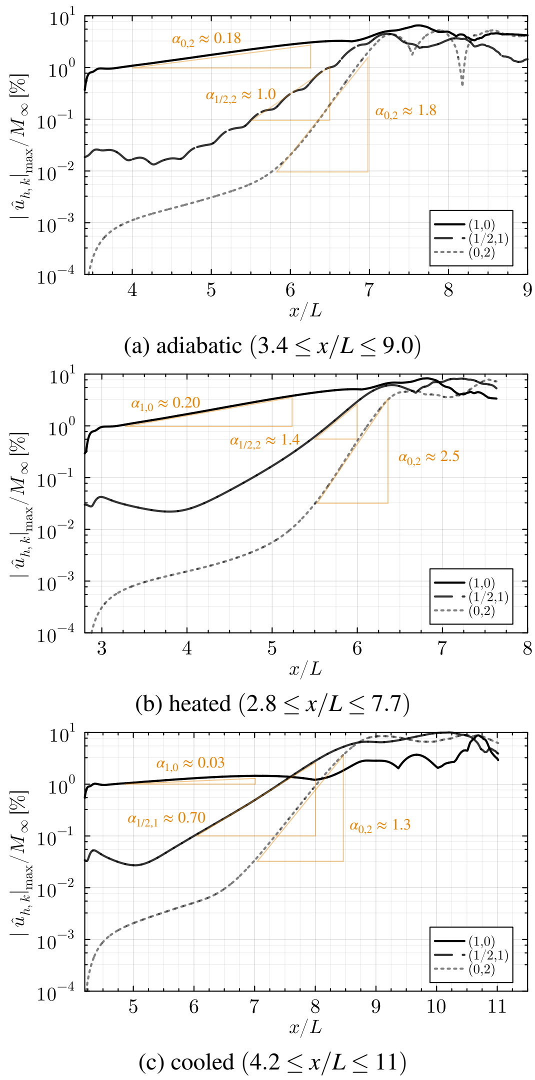

Figure 6. Streamwise growth of the maximum value Fourier amplitude of TS mode $(1,0)$, subharmonic oblique mode $(1/2,1)$, and vortex-streak mode $(0,2)$ for (1) adiabatic, (2) heated, and (3) cooled cases. The growth rates, $\alpha = (\log_{10}(b) - \log_{10}(a))/(b-a)$, are computed based on the orange triangles.

ture resulting from wall heat transfer be appropriately scaled? Also, as a consequence of the growth of steady vortex-streak mode $(0,2)$, the mean velocity profile is bent and the strong shear $\partial u/\partial y$ occurs. This strong shear causes the inflection point near-wall infection points near δ^* discussed in Figure 5. Although not shown here, we observed that the vortex-streak mode grows fastest along the displacement thickness distributions for all the cases. This indicates that the presence of GIPs near δ^* is the consequence of the emergence of the streak structure due to the growth of the vortex-streak mode $(0,2)$. In this viewpoint, additional pertinent questions emerge: How does heat transfer influence the inflectional instability triggered by streak growth? What causes the delay in the onset of inflectional instability between the boundary layer scale and the displacement thickness scale?

Summary

Direct numerical simulations (DNS) are performed to investigate the wall temperature impacts on the laminar-to-turbulent transition in a transonic boundary layer over a nominally zero-pressure-gradient flat plate. The freestream Mach number is 0.8, and the pseudo-adiabatic and the 10%-cooled/heated wall conditions are considered. The tiny wall-normal velocity disturbances consisting of a two-dimensional Tollmien–Schlichting (TS) wave and a subharmonic oblique wave are provided to induce the H-type transition. Currently, the following insights on wall temperature effects are obtained:

- Wall cooling attenuates the growth of TS mode subharmonic oblique wave, and vortex-streak mode, while wall heating promotes them.
- The three-dimensional structures become elongated, narrower, and flatter in the streamwise, spanwise, and wall-normal directions by wall cooling, whereas they shrunk, stretched, and lifted by wall heating.
- The wall temperature effects on the skin friction and shape factor profiles are distinct when the wall is cooled. The skin friction and the shape factor profiles present the two-stage evolution in the transitional regime. This is due to the lag in the onset of (generalized) inflection points of displacement thickness and boundary layer height scales.

ACKNOWLEDGEMENTS

This work was supported in part by the Japan Society for the Promotion of Science (JSPS) Grant-in-Aid for JSPS Fellows JP23KJ0167. Computer resources of the Fugaku supercomputer were provided by the RIKEN Advanced Institute for Computational Science through the HPCI System Research project (project ID hp230068, hp240083).

REFERENCES

Berlin, Stellan, Lundbladh, Anders & Henningson, Dan 1994 Spatial simulations of oblique transition in a boundary layer. *Phys. Fluids* **6** (6), 1949–1951.

Berlin, Stellan, Wiegel, Markus & Henningson, Dan S 1999 Numerical and experimental investigations of oblique boundary layer transition. *J. Fluid Mech.* **393**, 23–57.

Chang, Chau-Lyan & Malik, Mujeeb R 1994 Oblique-mode breakdown and secondary instability in supersonic boundary layers. *J. Fluid Mech.* **273**, 323–360.

Coleman, G N, Rumsey, C L & Spalart, P R 2018 Numerical study of turbulent separation bubbles with varying pressure gradient and reynolds number. *J. Fluid Mech.* **847**, 28–70.

Fasel, H F, Rist, U & Konzelmann, U 1990 Numerical investigation of the three-dimensional development in boundary-layer transition. *AIAA Journal* **28** (1), 29–37.

Gaitonde, Datta & Visbal, Miguel 1999 Further development of a Navier-Stokes solution procedure based on higher-order formulas. In *37th Aerospace Sciences Meeting and Exhibit*, *Aerospace Sciences Meetings* . American Institute of Aeronautics and Astronautics.

Hanifi, Ardeshir, Schmid, Peter J & Henningson, Dan S 1996 Transient growth in compressible boundary layer flow. *Phys. Fluids* **8** (3), 826–837.

Herbert, T 1988 Secondary instability of boundary layers. *Annu. Rev. Fluid Mech.* **20** (1), 487–526.

Kachanov, Y S & Levchenko, V Y 1984 The resonant interaction of disturbances at laminar-turbulent transition in a boundary layer. *J. Fluid Mech.* .

Klebanoff, P S, Tidstrom, K D & Sargent, L M 1962 The three-dimensional nature of boundary-layer instability. *J. Fluid Mech.* **12** (1), 1–34.

Lees, Lester & Lin, Chia-Chiao 1946 *Investigation of the Stability of the Laminar Boundary Layer in a Compressible Fluid*. National Advisory Committee for Aeronautics.

Lele, Sanjiva K 1992 Compact finite difference schemes with spectral-like resolution. *J. Comput. Phys.* **103** (1), 16–42.

Mack, L M 1984 Boundary-layer linear stability theory. *Agard rep* .

Mani, Ali 2012 Analysis and optimization of numerical sponge layers as a nonreflective boundary treatment. *J. Comput. Phys.* **231** (2), 704–716.

Masad, J A, Nayfeh, A H & Al-Maaitah, A A 1992 Effect of heat transfer on the stability of compressible boundary layers. *Comput. Fluids* **21** (1), 43–61.

Morkovin, Mark V 1969 On the many faces of transition. In *Viscous Drag Reduction*, pp. 1–31. Springer US.

Reshotko, Eli 1979 Drag reduction by cooling in Hydrogen-Fueled aircraft. *J. Aircr.* **16** (9), 584–590.

Rist, U & Fasel, H 1995 Direct numerical simulation of controlled transition in a flat-plate boundary layer. *J. Fluid Mech.* **298**, 211–248.

Schlichting, Hermann & Gersten, Klaus 2016 *Boundary-Layer Theory*. Springer.

Schmid, P J & Henningson, D S 1992 A new mechanism for rapid transition involving a pair of oblique waves. *Phys. Fluids* **4** (9), 1986–1989.

Shadloo, M S & Hadjadj, A 2017 Laminar-turbulent transition in supersonic boundary layers with surface heat transfer: A numerical study. *Numerical Heat Transfer, Part A: Applications* **72** (1), 40–53.

Sharma, S, Shadloo, M S & Hadjadj, A 2018 Laminar-to-turbulent transition in supersonic boundary layer: Effects of initial perturbation and wall heat transfer. *Numerical Heat Transfer, Part A: Applications* **73** (9), 583–603.

Spalart, Philippe R & Watmuff, Jonathan H 1993 Experimental and numerical study of a turbulent boundary layer with pressure gradients. *J. Fluid Mech.* **249**, 337–371.

Trefethen, L N, Trefethen, A E, Reddy, S C & Driscoll, T A 1993 Hydrodynamic stability without eigenvalues. *Science* **261** (5121), 578–584.

Unnikrishnan, S & Gaitonde, Datta V 2021 Instabilities and transition in cooled wall hypersonic boundary layers. *J. Fluid Mech.* **915**, A26.

White, F M & Majdalani, J 2006 *Viscous fluid flow*. McGraw-Hill.